Journal of Materials Chemistry A

REVIEW

View Article Online
View Journal | View Issue

Cite this: J. Mater. Chem. A, 2023, 11, 14614

Multi-functional photocatalytic systems for solar fuel production

Young Hyun Hong,[a] Yong-Min Lee, *[ab] Wonwoo Nam *[a] and Shunichi Fukuzumi *[ac]

Solar fuel production from water has received increasing attention due to increasing energy and environmental concerns. Herein we highlight dual- and multi-functional photocatalytic systems, which have both photosensitizing and thermal redox functions for solar fuel production. For example, polymeric cyano (CN)-bridged heteronuclear metal complexes act as dual functional photoredox catalysts that incorporate both a light harvesting photosensitizer and redox catalytic sites for the photocatalytic oxidation of water and reduction of dioxygen to produce H_2O_2. On the other hand, metal–organic frameworks (MOFs) contain both organic parts which act as photosensitizers and inorganic metal parts which act as redox catalysts, catalyzing water oxidation, H_2 evolution, CO_2 reduction and H_2O_2 production. An organic photoredox catalyst can be incorporated into nano-sized mesoporous cellular silica foams together with a redox catalyst for water oxidation, H_2 production, CO_2 reduction and H_2O_2 production. Finally, construction of multi-functional catalytic systems is discussed for solar-driven production of H_2 as molecular models of photosystem I (PSI) and photosystem II (PSII) in photosynthesis.

Received 20th April 2023
Accepted 7th June 2023

DOI: 10.1039/d3ta02356g

rsc.li/materials-a

1. Introduction

Fossil fuels that had been accumulated as products of photosynthesis on our planet have been consumed at a much faster rate than the current production of solar fuels by natural photosynthesis.[1] Such rapid consumption of fossil fuels has created concerns about global warming and climate change as well as their depletion in the near future.[2] Thus, an extensive effort has so far been devoted to produce solar fuels as

[a]Department of Chemistry and Nano Science, Ewha Womans University, Seoul 03760, Korea. E-mail: fukuzumi@chem.eng.osaka-u.ac.jp; yomlee@ewha.ac.kr; wwnam@ewha.ac.kr

[b]Research Institute for Basic Sciences, Ewha Womans University, Seoul 03760, Korea

[c]Department of Chemistry, University of Tsukuba, Tennodai, Tsukuba, Ibaraki 305-8571, Japan

Young Hyun Hong received her B.S. degree from the Department of Chemistry and Nano Science at Ewha Womans University, Korea, and Ph.D. degree from Ewha Womans University, Korea, under the supervision of Professor Wonwoo Nam and Professor Shunichi Fukuzumi in 2022. She is currently a post-doctoral fellow at Ewha Womans University.

Yong-Min Lee received his M.S. and Ph.D. degrees in Inorganic Chemistry from Pusan National University, Republic of Korea, under the supervision of Professor Sung-Nak Choi in 1999. After he worked in the Magnetic Resonance Centre (CERM) at the University of Florence, Italy, as a Postdoctoral fellow and Researcher under the direction of Professors Ivano Bertini and Claudio Luchinat from 1999 to 2005, he joined the Centre for Biomimetic Systems at Ewha Womans University, as a Research Professor in 2006. He is currently a Special Appointment Professor at Ewha Womans University since 2009.

renewable energy and material sources by artificial photosynthesis.[2–11] Artificial photosynthesis consists of light-harvesting and charge-separation units, combined with catalytic units for water oxidation and proton or CO_2 reduction, requiring multi-catalytic functions.[12–19] Semiconductor-based photocatalysts have been developed to realize multi-functional catalysis, which involves three steps:[20–32] (i) photoexcitation by photons with an energy greater than that of their band gap excites electrons to the conduction band, leaving holes in the valence band. (ii) The photogenerated electrons and holes are separated by overcoming coulombic attraction, followed by their diffusion and transfer. (iii) The surviving photogenerated electrons and holes react with adsorbed species on the surface of the photocatalyst for oxidation of water and reduction of protons or CO_2 with the use of cocatalysts combined with photocatalysts.[20–33] In the case of heterogeneous semiconductor-based photocatalysts, however, the detailed photocatalytic mechanisms have yet to be clarified because of the difficulty of identification and detection of reaction intermediates in heterogeneous systems in precluding rational molecular design for improvement of the catalytic efficiency and selectivity.[34]

In contrast, an extensive effort has been devoted to clarifying catalytic mechanisms of homogeneous water oxidation, proton or CO_2 reduction.[9–19,35–48] Dual functional homogeneous catalysts have been developed for photochemical synthesis.[49–54] However, multi-functional homogeneous photocatalysts have been less developed for photocatalytic water oxidation combined with proton or CO_2 reduction.

This review focuses on multi-functional photocatalytic systems for solar fuel production by combining photocatalytic water oxidation and proton or CO_2 reduction. Synthetic coordination polymer catalysts will be described, having dual catalytic functions, long-term stability, tolerance to experimental conditions, and good product selectivity including mechanistic investigations through *in situ* spectroscopy and kinetics. Metal–organic frameworks (MOFs) and mesoporous cellular silica foams containing both organic parts and inorganic metal parts will also be described inducing various photoredox reactions such as water oxidation, H_2 production, CO_2 reduction and H_2O_2 production. Then, immobilization of different molecular catalysts on solid-state supports for solar fuel production will be described to provide a system displaying dual catalytic function, enhanced selectivity and simplified identification of the active species, while also facilitating product isolation and catalyst recycling.[14,40,41,55] Finally, construction of multi-functional catalytic systems is discussed for solar-driven fuel production from water.[27,41–57]

2. Coordination polymeric cyano (CN)-bridged heteronuclear catalysts

Hydrogen peroxide has attracted increasing interest as a solar fuel that can be generated from H_2O and O_2 using solar energy and used in H_2O_2 fuel cells.[4,58–70] CN-bridged heteronuclear metal complex polymers ($M(II)[(bpy)Ru(II)(CN)_4]$: M(II) = Mn(II), Fe(II) and Ni(II); bpy = 2,2′-bipyridine: see Fig. 1) were reported

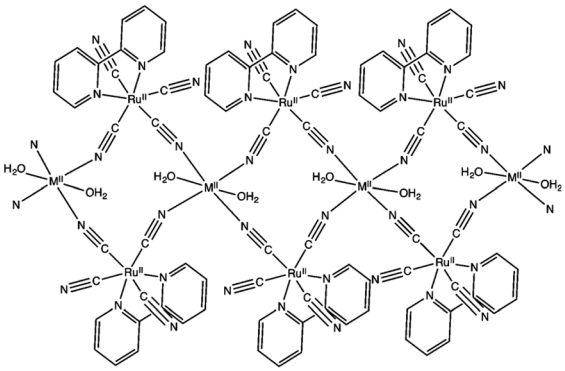

Fig. 1 Schematic structure of $M(II)[(bpy)Ru(II)(CN)_4]$. Reprinted from ref. 71 with permission from the Royal Society of Chemistry (Copyright 2017).

Wonwoo Nam earned his B.S. (Honours) degree in Chemistry from California State University, Los Angeles, and his Ph.D. degree in Inorganic Chemistry from the University of California, Los Angeles (UCLA) under the supervision of Professor Joan S. Valentine in 1990. After working as a postdoctoral fellow at UCLA for one year, he became an Assistant Professor at Hong Ik University in 1991. In 1994, he moved to Ewha Womans University, where he is currently a Distinguished Professor. His current research has been focused on dioxygen activation, water oxidation, and important roles of metal ions in bioinorganic chemistry.

Shunichi Fukuzumi earned a bachelor's degree and Ph.D. degree in applied chemistry at the Tokyo Institute of Technology in 1973 and 1978, respectively. After working as a postdoctoral fellow from 1978 to 1981 at Indiana University in the USA, he became an Assistant Professor in 1981 at Osaka University where he was promoted to a Full Professor in 1994. His research has been focused on electron transfer chemistry, particularly artificial photosynthesis. He is currently a Professor at Ewha Womans University and a Professor Emeritus at Osaka University.

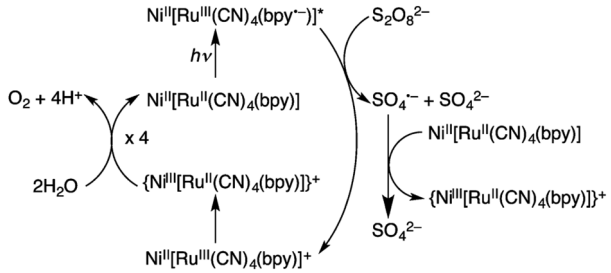

Scheme 1 Photocatalytic cycle of water oxidation by $S_2O_8^{2-}$ with Ni(II)[(bpy)Ru(II)(CN)$_4$]. Reprinted from ref. 71 with permission from the Royal Society of Chemistry (Copyright 2017).

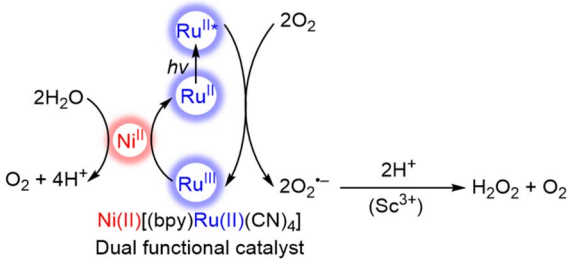

Scheme 2 Catalytic mechanism for the formation of hydrogen peroxide from water and dioxygen with a dual functional catalyst, Ni(II)[(bpy)Ru(II)(CN)$_4$], under visible light irradiation.[71]

to act as a dual functional photoredox catalyst for generation of H_2O_2 from H_2O and O_2 under visible light irradiation, catalyzing both photo-reduction of O_2 to H_2O_2 and photo-oxidation of H_2O to O_2.[71] The highest turnover number (TON) was obtained as 247 based on the monomer unit of Ni(II)[(bpy)Ru(II)(CN)$_4$] in the presence of Sc^{3+} under visible light irradiation.[71] As shown in Scheme 1, in the photocatalytic cycle it was proposed that electron transfer from {Ni(II)[(bpy)Ru(II)(CN)$_4$]}*, which is the excited state of Ni(II)[(bpy)Ru(II)(CN)$_4$], to $S_2O_8^{2-}$ occurs to afford {Ni(II)[(bpy)Ru(III)(CN)$_4$]}$^+$, $SO_4^{\bullet-}$ and SO_4^{2-}.[71] Then, {Ni(II)[(bpy)-Ru(III)(CN)$_4$]}$^+$ is converted to {Ni(III)[(bpy)Ru(II)(CN)$_4$]}$^+$.[71] Ni(II)[(bpy)Ru(II)(CN)$_4$] is also oxidized by $SO_4^{\bullet-}$ to form {Ni(III)[(bpy)Ru(II)(CN)$_4$]}$^+$, which oxidizes H_2O to evolve O_2.[71]

The photocatalytic oxidation of water with Ni(II)[(bpy)Ru(II)(CN)$_4$] is combined with the two-electron/two-proton reduction of O_2 to produce H_2O_2 from H_2O and O_2 in the presence of Sc^{3+} (Scheme 2).[71] Electron transfer from the photoexcited state of Ni(II)[(bpy)Ru(II)(CN)$_4$] to O_2 occurs in the presence of Sc^{3+} to afford {Ni(II)[(bpy)Ru(III)(CN)$_4$]}$^+$ and an $O_2^{\bullet-}$–Sc^{3+} complex that disproportionates in the presence of protons to form H_2O_2.[72–75] The dual-functional photocatalysis of a single catalyst M(II)[(bpy)Ru(II)(CN)$_4$] provides an efficient way to produce H_2O_2 from H_2O and O_2 as a promising solar fuel using sunlight.[71] The yields of H_2O_2 with M(II)[(bpy)Ru(II)(CN)$_4$] are summarized in Table 1, in which the maximum concentration of H_2O_2 obtained with the use of $Ni^{II}[Ru^{II}(CN)_4(bpy)]$ was 2.2 mM after 70 h of photoirradiation.[71]

A CN-bridged polynuclear metal complex containing iron(II) and ruthenium(II) incorporated in mesoporous silica–alumina {[Fe(II)$(H_2O)_3]_2$[Ru(II)$(CN)_6$]@sAl-MCM-41} was also reported to act as a dual-functional photocatalyst for the photocatalytic formation of H_2O_2 from H_2O and O_2 and oxidation of benzene (C_6H_6) to PhOH using O_2 as an oxygen source and as an oxidant under photoirradiation at 298 K.[76] [Fe(II)$(H_2O)_3]_2$[Ru(II)$(CN)_6$] exhibited catalytic activity in thermal hydroxylation of C_6H_6 by H_2O_2, where the apparent TON of PhOH formation reached ~390 for 60 h.[76] The TON increased to 2.5×10^3 for 114 h by incorporation of [Fe(II)$(H_2O)_3]_2$[Ru(II)$(CN)_6$] with sAl-MCM-41.[76] The iron ions in [Fe(II)$(H_2O)_3]_2$[Ru(II)$(CN)_6$] have extra H_2O ligands to form an octahedral coordination (Fig. 2).[76] The iron(II) ions may react with H_2O_2 to form hydroxyl radicals or iron-oxo species, which oxidize C_6H_6 to form PhOH.[76] [Fe(II)$(H_2O)_3]_2$[Ru(II)$(CN)_6$] acts as both an excellent catalyst for C_6H_6 hydroxylation with H_2O_2 to produce PhOH and also an effective photocatalyst for the H_2O oxidation with O_2 to generate hydrogen peroxide.[76]

The photocatalytic mechanism for generating H_2O_2 from H_2O and O_2 and hydroxylating C_6H_6 using a composite photocatalyst, [Fe(II)$(H_2O)_3]_2$[Ru(II)$(CN)_6$]@sAl-MCM-41, under irradiation is shown in Scheme 3.[76] Electron transfer from the

Table 1 Photocatalytic production of H_2O_2 from H_2O and O_2

Entry	Catalyst	Irradiated wavelength (nm)	Reaction conditions	H_2O_2 yield (h)	Ref
1	$Fe^{II}[Ru^{II}(CN)_4(bpy)]$	$\lambda > 390$ nm	O_2-saturated H_2O in the presence of $Sc(NO_3)_3$ (0.10 M) at 298 K	1.0 mM (300 h)	71
2	$Ni^{II}[Ru^{II}(CN)_4(bpy)]$	$\lambda > 390$ nm	O_2-saturated CH_3OH/H_2O (5 : 1, v/v) in the presence of $Sc(NO_3)_3$ (67 mM) at 298 K	2.2 mM (70 h)	71
3	$[Fe(H_2O)_3]_2[Ru(CN)_6]$@sAl-MCM-41	$\lambda > 390$ nm	O_2-saturated CH_3CN (2.9 mL) and H_2O (0.40 mL) in the presence of $Sc(NO_3)_3$ (0.10 M) at 298 K	3.0 mM (114 h)	76
4	$[Ru^{II}(Me_2phen)_3]^{2+}/[Ir(Cp^*)(H_2O_3)]^{2+}$	$\lambda > 420$ nm	O_2-saturated H_2O (3.0 mL) in the presence of $Sc(NO_3)_3$ (0.10 M) at 298 K	2.0 mM (23 h)	77
5	$[Ru^{II}(Me_2phen)_3]^{2+}/[Co(Cp^*)(bpy)(H_2O)]^{2+}$	$\lambda > 390$ nm	O_2-saturated H_2O (3.0 mL) in the presence of $Sc(NO_3)_3$ (0.10 M) at 298 K	1.1 mM (3 h)	58
6	MIL-125-NH_2 MOF	$\lambda > 420$ nm	O_2-saturated CH_3CN (5.0 mL)/H_2O (1.0 mL)	0.16 mM (20 h)	96
7	TTF–BT–COF	$\lambda > 420$ nm	O_2-saturated H_2O (10 mL) at 298 K	1.38 mM (1 h)	99

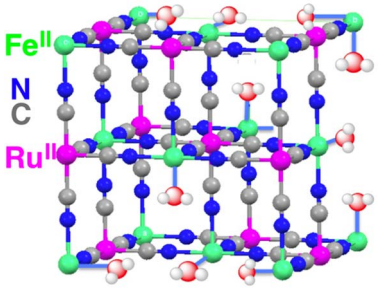

Fig. 2 Partial structure of $[Fe^{II}(H_2O)_3]_2[Ru^{II}(CN)_6]$. Reprinted from ref. 76 with permission from American Chemical Society (Copyright 2016).

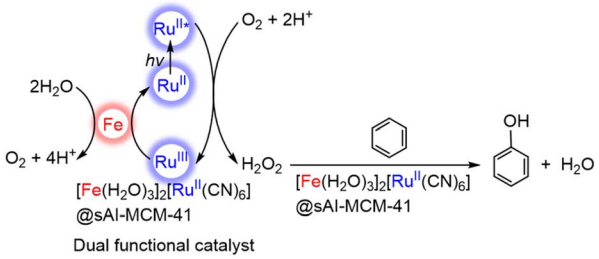

Scheme 3 Photocatalytic cycle for PhOH production from C_6H_6 and O_2 with $[Fe^{II}(H_2O)_3]_2[Ru^{II}(CN)_6]$@sAl-MCM-41.[76]

photoexcited state of $[Fe^{II}(H_2O)_3]_2[Ru^{II}(CN)_6]$ to O_2 occurs in the presence of Sc^{3+} to form $\{[Fe^{II}(H_2O)_3]_2[Ru^{III}(CN)_6]\}^+$ and $O_2^{\bullet-}$–Sc^{3+} species, which disproportionates in the presence of protons to yield H_2O_2.[76] The maximum concentration of H_2O_2 was 3.0 mM after 114 h of photoirradiation (entry no. 3 in Table 1).[76] The H_2O_2 concentration was higher than those obtained with the use of a combination of $[Ru^{II}(Me_2phen)_3]^{2+}$ with water oxidation catalysts (entry no. 3 and no. 4 in Table 1). H_2O_2 produced thus is used as an oxidant for hydroxylation of C_6H_6.[77,78] The combination of the photocatalytic H_2O_2 formation from H_2O and O_2 and the catalytic C_6H_6 oxidation to PhOH with H_2O_2 provides a new strategy to achieve single-pot C_6H_6 oxidation using O_2, which is an oxidant as well as an ideal oxygen source.[76]

A semiconductor–catalyst hybrid assembly has recently been synthesized for photocatalytic H_2O oxidation by forming CoFe Prussian blue (PB) particles on Dion–Jacobson type niobate (NB) nanosheets ($KCa_2Nb_3O_{10}$), which results in a p–n junction shown by the Mott–Schottky plot.[79] The assembly consisted of NB nanosheets and PB nanostructures with a particle size of about 50 nm.[79] Photocatalytic oxidation of H_2O was investigated on both bare NB nanosheets and the hybrid assembly in the presence of $S_2O_8^{2-}$, which is an electron scavenger, showing that the hybrid assembly exhibited greater photocatalytic activity (89.5 μmol g^{-1} h^{-1}) than NB nanosheets.[79] Various spectroscopic measurements, such as IR, XRD, XPS, SEM, and TEM, carried out on both raw and post-catalytic samples, showed that the hybrid assembly exhibited an appropriate band energy alignment for the photocatalytic H_2O oxidation process and was stable even after 12 h of photocatalytic experiments.[79] This implies that the hybrid assembly not only retained its structural integrity, but also enabled electron transfer between the NB nanosheets and PB units through charge transfer during the photocatalytic process.[79] As the hybrid assembly exhibited approximately 6.5 times higher catalytic activity than pure NB nanosheets, it can therefore be considered one of the first efficient p–n junction type NB hybrid assemblies with an earth-abundant cocatalyst.[79] The p–n junction feature allowed the hybrid assembly to be active in the UV as well as the visible region.[79] The facile restructuring of both NB nanosheets and PB particles with metal doping also allowed for several facile strategies to further explore NB/PB interaction.[79]

The moldability, wide composition, and compatibility with other substrates of coordination polymer materials as described above may enable achieving unique multi-catalytic functions for various photoredox reactions in the future.

3. Metal–organic frameworks

Metal–organic frameworks (MOFs) have been adopted to fabricate homogeneous polyoxometallate (POM) water oxidation catalysts (WOCs) as well as heterogeneous photosystems for recyclable utilization.[80–82] POM can be incorporated into MOF cavities to construct POM@MOF composites as a heterogeneous photocatalyst for photocatalytic water oxidation, where the MOF acts as a light harvester (Scheme 4).[15,83] It has been reported that a tetranuclear cobalt porphyrin (Porp–Co_4) is immobilized in the pores of porphyrin-linked zirconium MOF-545 to produce a Porp–Co_4 @MOF-545 complex for the photocatalytic oxidation of water.[84] The proposed mechanism is shown in Scheme 5.[84] First, the porphyrin captured the light and electron transfer from the excited state to the sacrificial electron acceptor occurred to produce the one-electron oxidized

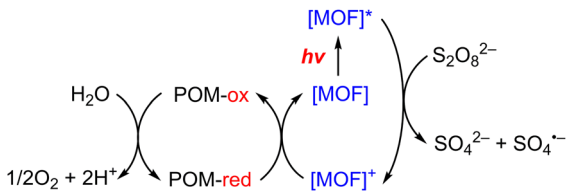

Scheme 4 Photocatalytic cycle of a Co_4–POM@MOF photosystem.[15]

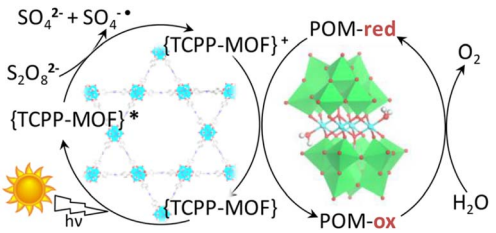

Scheme 5 Proposed mechanism for the light-driven water oxidation by Porp–Co_4@MOF-545. Reprinted from ref. 84 with permission from American Chemical Society (Copyright 2018).

porphyrin.[84] Then, Co_4–POM was oxidized and after 4 oxidizing equivalents on Co_4–POM, water was oxidized to evolve O_2.[84] The excellent performance of this photocatalytic system was attributed to the increase in the oxidative power of the MOF by the porphyrin ligand and the stabilization of the active site by confining Co_4–POM inside the pore of MOF-545.[84] Enhanced efficiency was achieved using Porp–Co_4 thin films on a TiO_2 support, which overcame the problems of the random orientation of the active sites and hindrance of light penetration.[85] Absorption capacity and charge separation at the Co_4–POM@MOF junction were increased by transferring electrons from the MOF to Co_4–POM to increase the efficiency.[85]

A Pt-loaded phosphorescent MOF was also utilized for efficient H_2 generation with higher turnover frequencies (TOFs) and an improved TON (7.0×10^3) compared to similar homogeneous catalysts.[73] [(bpy)Ir(III)(ppy)$_2$]Cl-derived dicarboxylic acids (H_2L_x in Fig. 3) were initially utilized for the successful synthesis of PtNP@MOFs (PtNP = Pt nanoparticle).[73] Internally grown octahedral nanocrystals were used to achieve H_2 evolution by electron injection into PtNPs and synergistic photoexcitation of the MOFs.[73]

A dinuclear iron complex, [FeFe](dcbdt)$(CO)_6$ (dcbdt = 1,4-dicarboxylbenzene-2,3-dithiolate), was incorporated into a highly robust Zr(IV)-based metal–organic framework (MOF), where postsynthetic ligand and metal ion exchange (PSE) occurred to construct UiO-66–[FeFe](dcbdt)$(CO)_6$, which is an organometallic, multinuclear, and nonprecious-metal-based proton reduction catalyst (Fig. 4).[86] UiO-66–[FeFe](dcbdt)$(CO)_6$ is a hybrid material that combines the highly stable and ordered inorganic support with the advantages of molecular catalysts.[86] The molecular integrity of the organometallic site in the MOF was confirmed by a variety of spectroscopic methods, including XAS.[86] Photocatalytic H_2 evolution occurs using ascorbate (Asc) as an electron donor, $[Ru^{II}(bpy)_3]^{2+}$ as a photosensitizer and MOF–[FeFe](dcbdt)$(CO)_6$ as a bifunctional photoredox catalyst (Scheme 6).[86] Incorporation of the Fe_2 complex in MOF–[FeFe](dcbdt)$(CO)_6$ resulted in higher stability under the photocatalytic conditions, protected the reduced species from charge recombination, and promoted the disproportionation

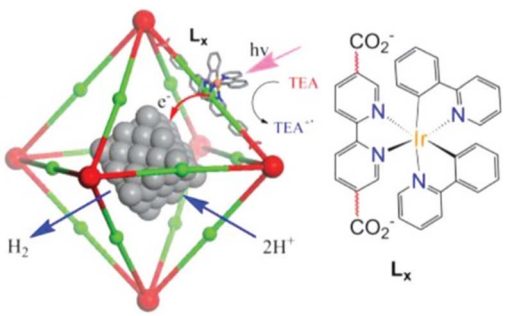

Fig. 3 Reaction scheme for the photocatalytic H_2 evolution *via* photoinjection of electrons from the light-harvesting MOFs into platinum NPs (PtNPs). The red and green balls represent $Zr_6(O)_4(OH)_4$(-carboxylate)$_{12}$ cores and the Ir–phosphor ligand of the MOFs, respectively. Reprinted from ref. 73 with permission from American Chemical Society (Copyright 2012).

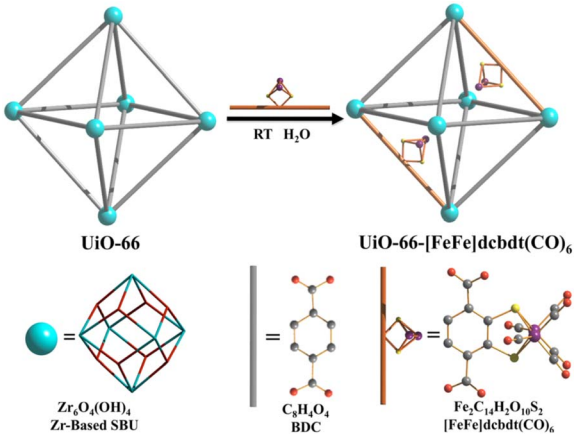

Fig. 4 Schematic representation of PSE of [FeFe](dcbdt)$(CO)_6$ into UiO-66. Reprinted from ref. 86 with permission from American Chemical Society (Copyright 2013).

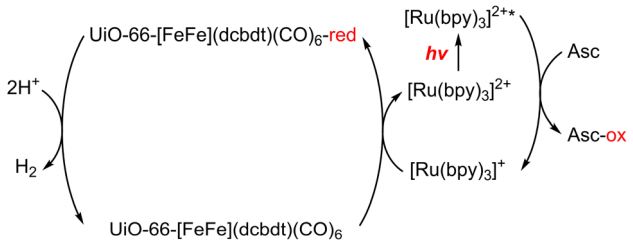

Scheme 6 Scheme for the photocatalytic H^+ reduction.[86]

reactions that generated catalytically active dianions.[86] Electron transfer from Asc to the photoexcited $[Ru^{II}(bpy)_3]^{2+}$ occurs to undergo photocatalytic H_2 evolution with UiO-66–[FeFe](dcbdt)$(CO)_6$.[86]

A POM-based $TBA_5[P_2Mo(V)_{16}Mo(VI)_8O_{71}(OH)_9Zn_8(L)_4]$ MOF (NNU-29), which exhibits strong chemical stability, can maintain the advantageous electronic properties of POM as well as keep the complex stable in aqueous solution.[87] In addition, the sensitive photocurrent response of this MOF enables a high separation efficiency of light-induced electron–hole pairs for the efficient heterogeneous photocatalytic conversion of CO_2 to HCO_2H in H_2O, reducing competitive H_2 generation (TON = 28).[88] Based on the analysis of the experimental results and theoretical calculations, the proposed mechanism for the photocatalytic conversion of CO_2 to HCOOH over NNU-29 is shown in Scheme 7.[88] When the photosensitizer $[Ru^{II}(bpy)_3]^{2+}$ is irradiated with visible light, an electron of $[Ru^{II}(bpy)_3]^{2+}$ is excited from HOMO to LUMO, and then transferred to NNU-29, resulting in reduction of NNU-29 and formation of $[Ru^{III}(bpy)_3]^{3+}$.[88] This is because NNU-29, which is like an electron sponge, can accept photoelectrons due to the valence change of several Mo atoms.[88] The POM moiety of reduced NNU-29 captures and reduces CO_2 and then returns to its original state.[88] Meanwhile, $[Ru^{III}(bpy)_3]^{3+}$ accepts an electron from TEOA as an electron donor and returns to $[Ru^{II}(bpy)_3]^{2+}$ while oxidizing TEOA.[88]

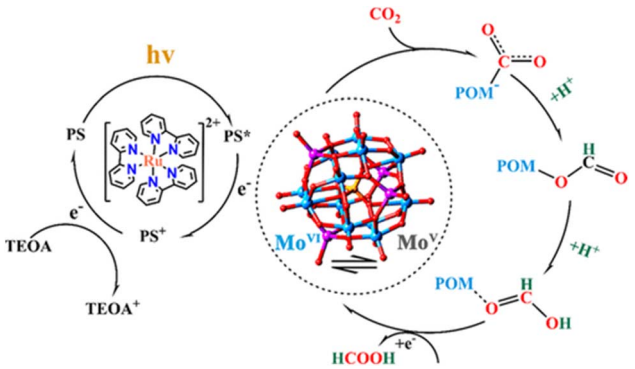

Scheme 7 Proposed mechanism for the photocatalytic CO_2 reduction to HCO_2H catalyzed by NNU-29. Reprinted from ref. 88 with permission from American Chemical Society (Copyright 2019).

In the latest study, the Keggin-type polyoxometalate (POM) $PW_{12}O_{40}^{3-}$ and an Rh catalyst Cp*Rh(bpydc)Cl_2 (bpydc = 2,2′-bipyridine-5,5′-dicarboxylic acid) in the UiO MOF (PW_{12},Cp*Rh)@UiO-67 demonstrated high photocatalytic activity for CO_2 reduction to produce formate (Scheme 8).[89] Compared to that observed for the Cp*Rh@UiO-67 catalyst without POM, the production of formate was doubled and achieved a maximum TON of 175 when fabricated as thin films, demonstrating the beneficial effect of POM.[89] However, PW_{12} has a minimal effect on the electronic structure of the composite but acts as a proton relay.[89]

Photocatalytic reduction of CO_2 into value added fuel (*i.e.*, CO) together with reduction of H^+ to H_2 using an Fe(III)(TCPP)@NU-1000 catalyst was reported by Hupp and co-workers.[90] The Fe(III)(TCPP)@NU-1000 catalyst was prepared by grafting an iron(III)–porphyrin (Fe(III)(TCPP); TCPP = tetrakis(4-carboxyphenyl)porphyrin) onto the hexagonal portion of the NU-1000 MOF mesopore.[90] This catalyst was available in the 8-connected nodes, giving a TON of ~20 for both products, CO and H_2, under light for 2 h.[90] Hupp and co-workers also addressed the problem of catalyst leaching from the chromophoric MOF after the TON reached 20 and discussed the need to design better linkers or binding sites to improve catalyst robustness as well as increase TON.[90] The mechanism of the photocatalytic reduction of CO_2 with Fe(III)(TCPP)@NU-1000 was proposed as shown in Scheme 9.[90,91] In the presence of TEOA as a sacrificial reductant, the photoexcited electrons were transferred initially from NU-1000* to Fe(III)(TCPP) to generate Fe(I)(TCPP), followed by reformation of NU-1000 and production of $TEOA^+$.[90] In the presence of a second molecule of TEOA, spontaneous decomposition of $TEOA^+$ generated a strongly reducing radical species with $TEOAH^+$.[92–94] The resulting radical species could donate the electron required to reach the catalytically active Fe(0)(TCPP) species.[90] Alternatively, disproportionation of two Fe(I)(TCPP) molecules to Fe(II)(TCPP) and Fe(0)(TCPP) could effectively double the number of available reducing equivalents, when the radical species that is the decomposition product of $TEOA^+$ reduces Fe(II)(TCPP) to Fe(I)(TCPP).[90] Then, CO_2 is bound to Fe(0)(TCPP) species to produce a Fe(0)(TCPP)–CO_2 adduct species, which is susceptible to further reaction to generate Fe(II)(TCPP)–CO.[90] Released O^{2-} reacts with protons from TEOA (or contingent sources) to produce H_2O.[90] When CO was released from Fe(II)(TCPP)–CO, Fe(II)(TCPP) was regenerated and the next catalytic cycle started again.[90] As a competing process, Fe(0)(TCCP) may convert H^+ to H^- to form an iron(II)-hydride complex that reacts with an additional proton to give H_2.[90]

A microporous anthracene-functionalized Zr-MOF (NNU28) was prepared as a dual functional photoredox catalyst for reduction of CO_2 to produce formate.[95] Zr-MOF demonstrated efficient photoinduced charge generation, broadband visible light absorption, and high CO_2 absorption, along with excellent chemical and thermal stability.[95] NNU28 exhibited the highest rate of formation of formate (~180 μmol h^{-1} mmol$(MOF)^{-1}$) among Zr-based MOF photocatalysts.[95] The Zr_6 oxo cluster and anthracene-based organic ligand both act as photocatalytic centers for CO_2 reduction under visible irradiation.[95] The dual photocatalytic pathways for photoreduction of CO_2 with NNU28

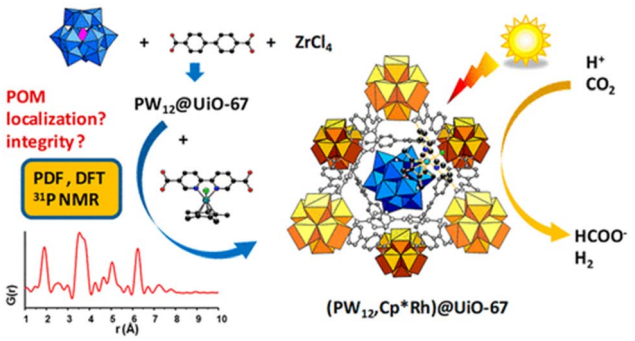

Scheme 8 Scheme for photocatalytic reduction of CO_2 to produce formate catalyzed by (PW_{12},Cp*Rh)@UiO-67. Reprinted from ref. 89 with permission from American Chemical Society (Copyright 2020).

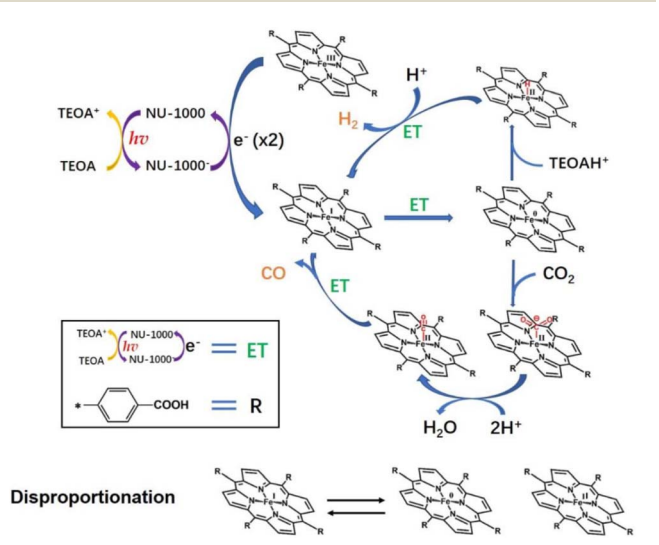

Scheme 9 Proposed mechanism for photocatalytic reduction of CO_2 using an Fe–TCPP@NU-1000 heterogeneous catalyst with TEOA as a sacrificial agent. Reprinted from ref. 90 with permission from Elsevier (Copyright 2022).

were demonstrated to be generally more efficient for visible-light-driven CO_2 reduction than that typically relying on a ligand-to-metal charge transfer process, illustrating a new strategy to design and synthesize novel visible-light photocatalysts for CO_2 reduction with high efficiency.[95] A photocatalytic mechanism of dual catalytic pathways for photoreduction of CO_2 with NNU28 is shown in Scheme 10.[95] Upon photoirradiation, the anthracene-based ligand in NNU28 acts as an efficient visible light harvester for the sensitized Zr_6 oxo cluster *via* the ligand-to-metal charge transfer (LMCT) process, undergoing photoinduced electron transfer from TEOA.[95] The two catalytic pathways in Scheme 10 contribute to the photoreduction of CO_2 to formate, accounting for the high catalytic performance of NNU28.[95] The large conjugation of the anthracene-based ligand resulted in unexpected optical performance for the MOFs.[95]

Visible light-driven $2e^-$ O_2 reduction to H_2O_2 with TEOA or benzyl alcohol was also catalyzed by a metal–organic framework (MIL-125-NH_2).[96] When NiO nanoparticles (NPs) were deposited onto MIL-125-NH_2, the photocatalytic reduction of O_2 to H_2O_2 was dramatically enhanced through disproportionation of $O_2^{\bullet-}$ (Scheme 11).[96] NiO acted as a WOC when water was used as a source of electrons.[96] The H_2O_2 concentration was 0.16 mM after 20 h photoirradiation (entry no. 6 in Table 1). The photocatalytic mechanism of generation of H_2O_2 by $2e^-$ O_2 reduction with TEOA catalyzed by NiO/MIL-125-NH_2 is shown in Scheme 11.[96] Photoexcitation of MIL-125-NH_2 results in production of $Ti_8O_8(OH)_4^{\bullet-}$ and a hole at the linker.[97,98] The produced hole is quenched by electron transfer from TEOA, followed by O_2 reduction with $Ti_8O_8(OH)_4^{\bullet-}$ to produce $O_2^{\bullet-}$ that disproportionates with H^+ to yield H_2O_2.[96]

Photocatalytic production of H_2O_2 by combination of H_2O oxidation and O_2 reduction to H_2O_2 without sacrificial agents is highly required (*vide supra*).[99] A redox molecular-conjugated COF (TTF–BT–COF) was synthesized through the covalent bonding of tetrathiafulvalene (TTF) as a photooxidation site and benzothiazole (BT) as a photoreduction site.[99] This photocatalyst was applied to the generation of H_2O_2 without sacrificial agents (Scheme 12).[99] The concentration of H_2O_2 reached 1.38 mM after 1 h of photoirradiation (entry no. 7 in Table 1).[99] The covalent linkage between them creates a redox junction, providing appropriate photo-redox ability, effective electron–hole separation efficiency, and visible light adsorption, allowing effective visible light-driven electron transfer from BT to TTF, resulting in the simultaneous WOR and ORR.[99] It is worth noting that the production rate (276 000 $\mu M\ h^{-1}\ g^{-1}$) for H_2O_2 photoproduction without sacrificial donors can be record-high among porous crystalline photocatalysts, approximately 10 times higher than that with single linkers or physical mixtures.[99] In addition, theoretical calculations have demonstrated redox molecular junctions that can enhance the performance by facilitating charge transfer and significantly reducing the energy barriers of both the WOR and ORR.[99] This is the first research capable of designing redox molecular junction COF for production of H_2O_2, potentially shedding new light on the exploration of porous crystalline materials in industrial scale H_2O_2 production.[99]

Carbon-based semiconductors and graphic carbon nitride (g-C_3N_4) and graphene oxide systems have also been frequently

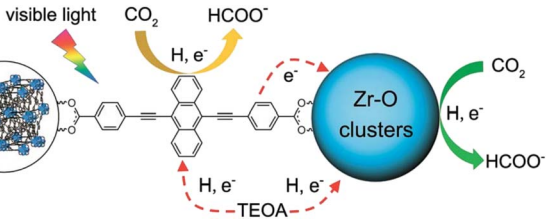

Scheme 10 A photocatalytic scheme for CO_2 reduction by TEOA with NNU28 under visible irradiation. Reprinted from ref. 95 with permission from the Royal Society of Chemistry (Copyright 2016).

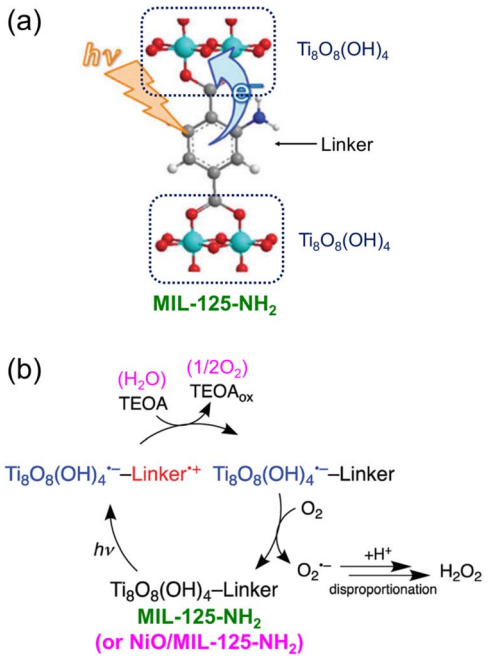

Scheme 11 Visible light-driven $2e^-$ O_2 reduction to H_2O_2 with TEOA catalyzed by Ni/MIL-125-NH_2. Reproduced from ref. 96 with permission from the Royal Society of Chemistry (Copyright 2018).

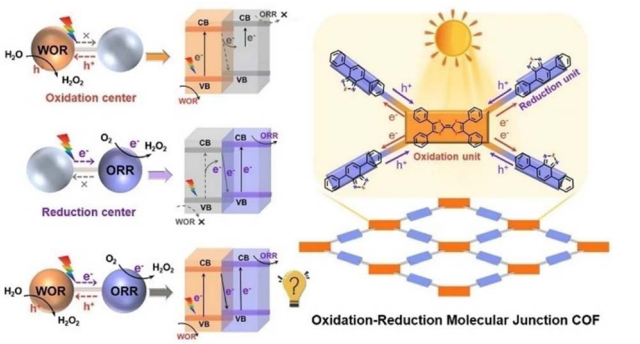

Scheme 12 Schematic diagram for H_2O_2 formation with a redox molecular-conjugated COF photocatalyst. Reprinted from ref. 99 with permission from John Wiley and Sons (Copyright 2023).

used for photocatalytic production of H_2O_2 from H_2O and O_2.[67,100–102] These heterogeneous materials may not be suitable to combine molecular catalysts to develop multi-catalytic functions. In contrast, the multi-catalytic functions of the COF and MOF can be further expanded because the COF and MOF have not only the intrinsic catalytic activity but also the capability to encapsulate additional catalytic sites.

4. Mesoporous cellular silica foams

Numerous photocatalytic systems of interest have been developed by utilizing mesoporous silica, which has high stability due to its robust structural framework, confinement effects inside the channels with controllable hydrophobicity/hydrophilicity, and high specific surface area with uniform pore size.[28,103–115]

Recently, Inagaki and co-workers reported photocatalytic water splitting for the oxygen evolution reaction (OER) with the use of periodic mesoporous organosilica (PMO) grafted with a $[Ru(II)(bpy)_3]^{2+}$ sensitizer.[116] The unique pore-wall structure (bpy-PMO) in the PMO pores is responsible for the generation of photoredox-active metal complexes on the outer surface of the material (Scheme 13).[116]

Inagaki and co-workers also reported fine-tuning of the photocatalyst to increase the photocatalytic rate up to 20 times under visible light irradiation.[116] The photochemical properties of the catalyst ($Ru(II)(X_2bpy)_3$/PMO) were controlled by changing the 4,4′-di-X substituents of the bpy ligand (X_2bpy = 4,4′-X-2,2′-bipyridine) in the PMO framework, where X = H, Me, ^{t}Bu, and C(O)OMe.[116]

The mesospaces uniformly distributed among Al–SiO_2NPs were utilized to construct a self-assembled and active catalytic structure of 2-phenyl-4-(1-naphthyl)quinolinium ion ($QuPh^+$-NA) and PtNPs for photocatalytic H_2 evolution in artificial photosynthetic systems at room temperature.[117] This composite catalyst (PtNPs/$QuPh^+$-NA/Al–SiO_2NPs) was synthesized using an aqueous suspension of PVP-capped PtNPs and an MeCN solution of $QuPh^+$-NA by sequential addition to the aqueous dispersion of Al–SiO_2NPs and then by placing it in an ultrasonicator for 30 min.[117] The mesospaces allowed the controlled incorporation of PtNPs surrounded by several $QuPh^+$-NA ions and the surface of the Al–SiO_2NPs was covered with $QuPh^+$-NA ions as shown in Fig. 5.[117] This mesoporous structure allowed

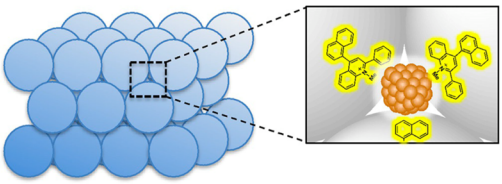

Fig. 5 Structure of the catalyst prepared with silica–alumina NPs (Al–SiO_2NPs) supporting $QuPh^+$-NA on silica–alumina and PtNPs. Reproduced from ref. 117 with permission from John Wiley and Sons (Copyright 2016).

the PtNP to receive multiple electrons from $QuPh^{\bullet}$-NA species, which were produced by electron transfer from β-dihydronicotinamide adenine dinucleotide (NADH) to the $QuPh^{\bullet}$-$NA^{\bullet+}$ (photoinduced ET state of $QuPh^+$-NA ions). As a result, H_2 was efficiently produced photocatalytically, and the catalyst was recycled multiple times.[117] In contrast to the case of the PtNPs/$QuPh^+$-NA/Al–SiO_2NPs catalyst, almost no H_2 formation was observed in the conventional mesoporous silica–alumina photocatalytic reaction system containing $QuPh^+$-NA ions together with PtNPs instead of the PtNPs/$QuPh^+$-NA/Al–SiO_2NPs catalyst under the same reaction conditions.[114] PtNPs with a size of 2 nm were too large to interact with $QuPh^+$-NA ions immobilized inside the cylindrical mesopores, resulting in no photocatalytic H_2 formation.[114] Self-assembled structures of such metal oxide NPs are a promising platform for the assembly of functional organic compounds and NPs.[114]

Liu and co-workers reported that a $[(Cp^*)Ir^{III}Cl(\mu\text{-}Cl)]_2$ complex was immobilized on bipyridine-based organosilica NTs (bpy/ENT) to obtain an organic–inorganic hybrid solid photocatalyst (Ir-bpy/ENT) for photocatalytic H_2 evolution from both formate and aldehyde (Scheme 14).[118] Ir-bpy/ENT has high surface area, stable nanotube structure, and confining effects inside its channels due to its large pore diameter, reducing diffusion inhibition and facilitating the facile transport of substrates, which is an important function to enhance the catalytic reactivity (Scheme 14).[118] In addition, Ir-bpy/ENT has

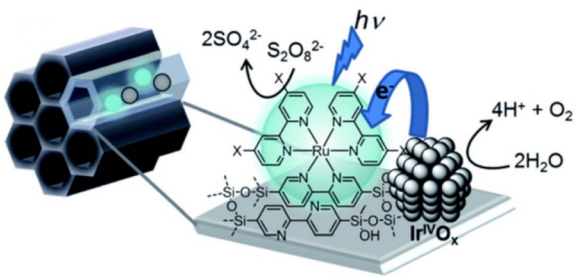

Scheme 13 Photocatalytic water oxidation by Ru complexes supported on BPy-PMO. Reprinted from ref. 116 with permission from the Royal Society of Chemistry (Copyright 2020).

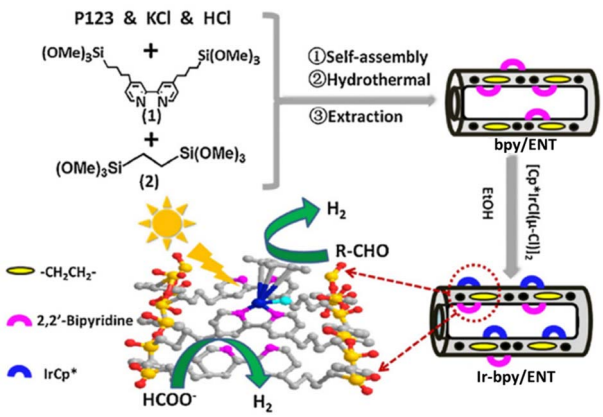

Scheme 14 Synthesis of Ir-bpy/ENT and photocatalysis with Ir-bpy/ENT, where ENT is an ethenyl-bridged organosilica nanotube. Reprinted from ref. 118 with permission from Elsevier (Copyright 2018).

controllable hydrophobicity/hydrophilicity and isolated active sites.[118] Ir-bpy/ENT can also provide high efficiency in the pH-dependent production of pure H_2 (TOF = 16.2 h^{-1} and QY = ~8.0%) from formate.[118] The Ir-bpy/ENT catalyst can be reused up to 6 cycles.[118]

Li and co-workers immobilized a Co(III) cyclam complex (cyclam = 1,4,8,11-tetraazacyclotetradecane) on the surface of mesoporous silica with the use of two different covalent linkages (Fig. 6).[119] Li and co-workers also reported a heterogeneous photocatalyst designed for the photocatalytic reduction of CO_2 to CO in the presence of *p*-terphenyl as a molecular photosensitizer.[119] A TON of 12.5 for CO formation was achieved using Co(L)/SiO_2 after CO_2 reduction. Using one of the modified Co^{III}(cyclam)X/SiO_2, the TON of CO formation reached 160 in the photocatalytic CO_2 reduction.[119]

Various photocatalysts were embedded with PMO to afford abundant organic molecules (R) immobilized to the silica framework as light harvesters (Fig. 7a).[120,121] 10-Me-acridone groups able to absorb visible light were used as R in the PMO framework.[121] The silica units interact strongly with the phosphonic acid groups of the PRu-Re photocatalyst, trapping PRu-Re inside PMO, resulting in a hybrid catalyst (Fig. 7b).[121] The photons harvested by about 40 molecules of 10-Me-acridone were transferred to a Ru(II) unit of a PRu-Re photocatalyst in the hybrid catalyst, and then the photocatalytic CO_2 reduction was initiated.[121] The PMO hybrid with a light-harvesting function showed a 10-fold increase in the photocatalytic CO release rate compared to the PRu-Re-adsorbed PMO without a light harvester.[121] When a benzimidazoline derivative was used as an electron donor in the photocatalytic CO_2 reduction, the apparent TON for CO formation was more than 600.[121]

On the other hand, a multi-functional hybrid catalyst material was obtained by incorporating a 9-mesityl-10-methylacridinium ion (Acr^+-Mes)[47] into mesoporous silica–alumina, in which a copper complex [Cu(II)(TPA)]$(ClO_4)_2$ (TPA = tris(2-pyridylmethyl)amine) was embedded by cation exchange.[122] The hybrid composite catalyst $[Cu(II)(TPA)]^{2+}$/Acr^+-Mes@AlMCM-41 acted as an efficient and robust photocatalyst in the oxidation of *p*-xylene by O_2 to yield 4-Me-benzaldehyde selectively and H_2O_2.[122] A nano-sized mesoporous silica–alumina (sAlMCM-41 and tAlMCM-41) also stabilizes the electron-transfer state of Acr^+-Mes, which is an electron donor–acceptor dyad cation.[122] Acr^+-Mes was easily incorporated into nano-sized mesoporous silica–alumina to produce a composite

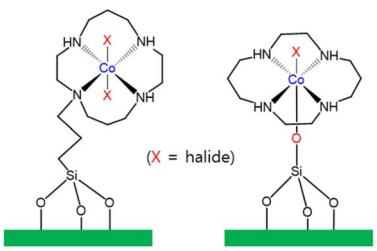

Fig. 6 Co(L)/SiO_2 bearing a cyclam ligand, showing two different covalent linkages.[119]

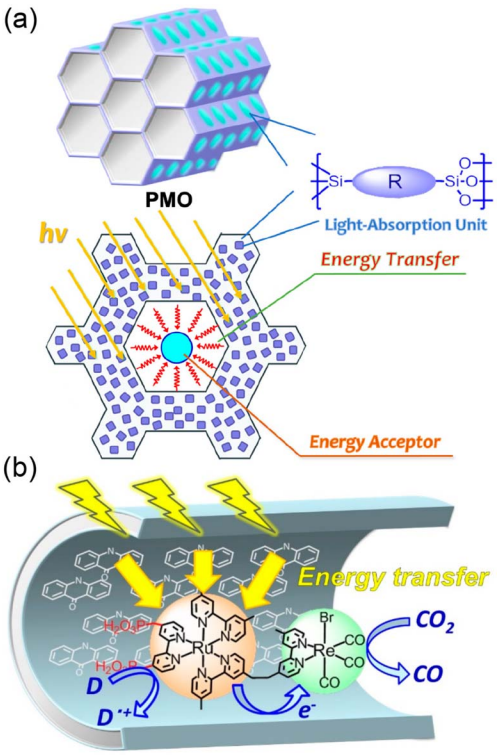

Fig. 7 (a) Structural arrangement of each part of the PMO. (b) Photocatalytic CO_2 reduction by light harvesting hybrids of PRu-Re and 10-Me-acridone in PMO. Reprinted from ref. 121 with permission from American Chemical Society (Copyright 2022).

by a cation-exchange reaction.[122] Photoexcitation of sAlMCM-41 and tAlMCM-41 resulted in generation of an extremely long-lived $Acr^{\bullet}$-$Mes^{\bullet+}$, which is an electron-transfer state, as detected by EPR and laser induced transient absorption measurements.[122] $Acr^{\bullet}$-$Mes^{\bullet+}$ incorporated into tAlMCM-41 also has a very long lifetime lasting over 1 s at ambient temperature and decays *via* intramolecular back electron transfer as opposed to the diffusion-limited intermolecular back electron transfer between two $Acr^{\bullet}$-$Mes^{\bullet+}$ molecules in solution.[122]

The photocatalytic mechanism for the oxidation of *p*-xylene with $[Cu(II)(TPA)]^{2+}$/Acr^+-Mes@AlMCM-41 is shown in Scheme 15.[122] First, photoexcitation of Acr^+-Mes@AlMCM-41 results in formation of the long-lived $Acr^{\bullet}$-$Mes^{\bullet+}$, followed by electron transfer from *p*-xylene to the $Mes^{\bullet+}$ moiety of $Acr^{\bullet}$-$Mes^{\bullet+}$.[122] The radical cation, which is 1 e^- oxidized species of *p*-xylene, thus deprotonates to form a 4-Me-benzyl radical, which reacts rapidly with O_2 to produce a 4-Me-benzylperoxyl radical.[122] Then, 4-Me-benzylperoxyl radical disproportionates to form 4-Me-benzyl alcohol, 4-Me-benzaldehyde and O_2.[122] 4-Me-benzyl alcohol was further oxidized *via* electron transfer from 4-Me-benzyl alcohol to the $Mes^{\bullet+}$ moiety of $Acr^{\bullet}$-$Mes^{\bullet+}$ to produce 4-Me-benzaldehyde selectively as the final oxygenated product of *p*-xylene.[123] On the other hand, the reduction of O_2 by $Acr^{\bullet}$-Mes is catalyzed by $[Cu(II)(TPA)]^{2+}$.[122] The incorporation of Acr^+-Mes into nano-sized mesoporous silica–alumina coupled with $[Cu(II)(TPA)]^{2+}$ as an O_2 reduction catalyst presented a promising way to develop efficient and robust organic photocatalysts

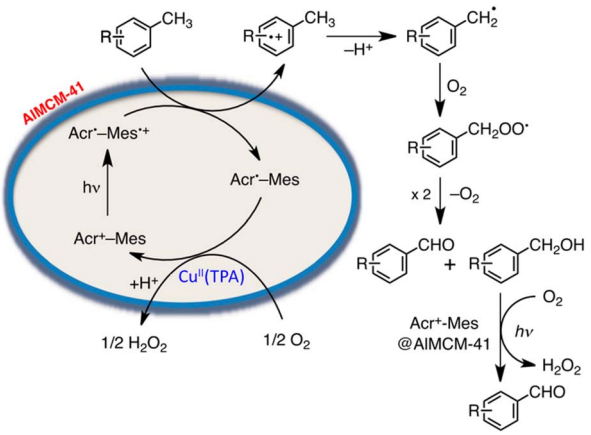

Scheme 15 Photocatalytic mechanism for the oxidation of *p*-xylene selectively by O_2 with $[Cu(II)(TPA)]^{2+}$/Acr^+-Mes@AlMCM-41. Reprinted from ref. 122 with permission from the National Academy of Sciences (Copyright 2012).

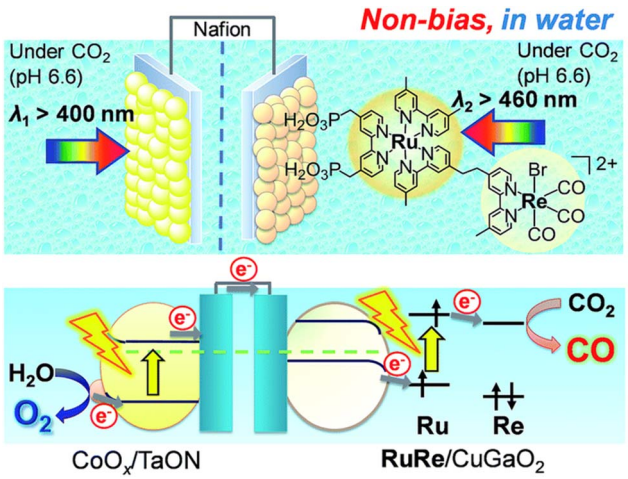

Scheme 16 Schematic image of a hybrid photoelectrochemical cell in a Z-scheme configuration. Reprinted from ref. 132 with permission from the Royal Society of Chemistry (Copyright 2017).

combined with a metal complex catalyst, which acts as a multi-functional catalytic material for the oxidation of the substrate by O_2 that is the ultimate environmentally benign oxidant in artificial photosynthesis to produce solar fuels.[123]

Immobilization of different functional catalysts in mesoporous silica–alumina may enable the development of more efficient multifunctional catalytic systems in the future.

5. Hybrid photoelectrochemical cell

Hybrid photoelectrochemical cells composed of metal complexes and semiconductor materials with relatively high photochemical oxidation power have recently been developed for visible-light-driven multi-functional solar fuel production.[124–131] Photocatalysts with semiconductor particles afford both high selectivity and strong oxidation power by photoexcitation of both the redox photosensitizer and the semiconductor *via* the so-called Z-scheme mechanism.[124–131]

A Z-scheme configuration of a hybrid photoelectrochemical cell composed of a RuRe/$CuGaO_2$ photocathode and a CoO_x/TaON photoanode has been constructed to perform CO_2 reduction by H_2O without bias potential as shown in Scheme 16.[132,133] Two compartment cells that contain a CO_2-saturated electrolyte solution were separated using a Nafion membrane.[132] Visible light irradiation of the RuRe/$CuGaO_2$ photocathode and the CoO_x/TaON photoanode in the wavelength region of λ_{ex} > 460 nm and λ_{ex} > 400 nm, respectively, resulted in formation of reduced products (CO and H_2) and O_2 (the four-electron oxidized product of water) in the cathode and anode cells, respectively.[132] The amount of CO produced was 232 nmol and the TON_{CO} reached 22 based on the amount of immobilized RuRe.[132] The hybrid photoelectrochemical cell made it possible to reduce CO_2 to CO as well as to oxidize water to O_2 by photoexcitation of both RuRe and TaON *via* a Z-scheme-type electron transfer under visible-light irradiation.[132]

On the other hand, a p-type nickel oxide (NiO) photocathode was modified with a hexaphosphonated $Ru(bpy)_3$-based dye (RuP_3) that is linked with a tetraphosphonated molecular $[Ni(P_2N_2)_2]^{2+}$ type proton reduction catalyst (NiP) to be employed for the photocatalytic H_2 evolution in water (Scheme 17).[134] By using a layer-by-layer deposition method, Zr^{4+}-phosphonates were linked to the phosphonate units of RuP_3 and NiP in a supramolecular assembly on the p-type semiconductor NiO photocathode.[134] Such a layer-by-layer method made it possible to control spatial arrangement of individual units without elaborate chemical synthesis of the dye–linker–catalyst dyad,[134] keeping the dye located close to the catalyst and semiconductor

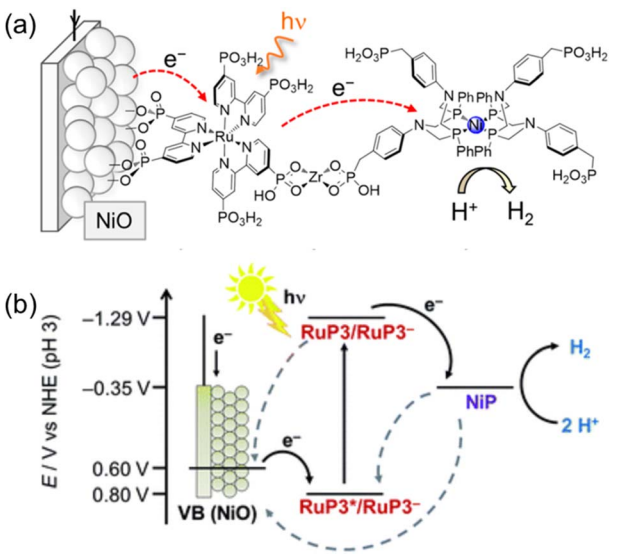

Scheme 17 (a) Schematic procedure of sequential immersion of Zr^{4+} bridge-based photocathodes (NiO|RuP_3–Zr^{4+}–NiP). (b) Energy diagram of photoinduced electron injection from a NiO photocathode to the excited state of RuP_3. Back solid arrows show forward electron transfer and grey dashed arrows show possible recombination pathways between p-NiO, RuP_3 and NiP. Reprinted from ref. 134 with permission from the Royal Society of Chemistry (Copyright 2016).

surface to facilitate the photocatalytic activity, but spatially separating NiP from NiO to avoid charge recombination.[134] The NiO|RuP_3–Zr^{4+}–NiP electrodes generate higher and more stable photocurrents as compared to photocathodes with RuP_3 and NiP co-immobilized on the NiO surface in the absence of Zr^{4+} cations linking the dye and catalyst.[134] Directed electron transfer from the excited dye to the catalyst occurs efficiently, whereas charge recombination was slowed down in the dye–linker–catalyst dyad.[134] Thus, photoelectrocatalytic generation of H_2 occurred at the NiO|RuP_3–Zr^{4+}–NiP hybrid electrode at an electrochemical underpotential, thereby demonstrating the potential of this photoelectrocatalytic system to store light in the chemical bonds of H_2.[134]

The efficiency of the NiO|RuP_3–Zr^{4+}–NiP electrodes may be improved by developing phosphonated push–pull dyes optimized for the photoelectrocatalytic H_2 evolution.[135] Further work may also include the synthesis and investigation of dyes, which are more suitable for injecting holes into the NiO valence band.[135] Thus, the multifunctions of light-harvesting, electron transfer and H_2 evolution catalytic functions can be further optimized.

6. Multi-functional molecular models of photosystems in photosynthesis

Much attention has been paid to the design of direct Z-scheme photocatalysts for solar energy conversion due to their effectiveness in spatially separating photogenerated electron–hole pairs and optimizing the oxidation and reduction capabilities of the photocatalytic system.[136–145] In natural photosynthesis, water oxidation is a major reaction using a Mn_4CaO_5 cluster under solar illumination in photosystem II (PSII).[146–149] In PS II, photocatalytic water oxidation evolves O_2 with the supply of electrons and protons for solar fuel production.[150] Photoexcited chlorophyll aggregates, P680*, undergo charge separation and electrons are transferred to quinones (Q_A and Q_B).[151] Finally plastoquinone (PQ) accepted electrons to produce plastoquinol (PQH_2) by taking two protons from its surroundings.[152,153] As one molecule of plastoquinone is oxidized, two electrons are transferred to P700. Photosystem I (PSI) has the photooxidation and reduction cycle of P700.[154] In this cycle, the electron flows to $NADP^+$ to produce NADPH through electron carriers.[155] In photosynthetic linear electron flow, the so-called Z-scheme, electrons that came from H_2O oxidation in photosystem II are transferred to $NADP^+$ to produce NADPH. On the other hand, in the dark reaction, driven by the energy stored in ATP, CO_2 is finally stepwise reduced into carbohydrates.[156] Light energy is stored in the form of NADPH, while some of the light energy is stored in the form of ATP through the phosphorylation of ADP.[157,158] That is, the overall process of photosynthesis is the process of producing organic compounds such as carbohydrates by the reduction of CO_2 along with the oxidation of water.[157,158]

Inspired by the Z-scheme in photosynthesis, photocatalytic water splitting was achieved with the use of molecular catalysts.[159] The combination of PSI and PSII models achieved photocatalytic H_2O splitting for the first time, allowing the production of O_2 and H_2 in a ratio of 1 : 2 (Scheme 18).[159] As shown in Fig. 8, each molecular model of photosystem, PSI or PSII, contains two solvent phases, toluene ($PhCH_3$) and water/trifluoroethanol mixture (H_2O/TFE, 3 : 1) phases, which are separated using a liquid membrane.[159] The $PhCH_3$ and H_2O/TFE mixture phases of the PSII functional model were each connected to the same phase of the PSI functional model using two glass membranes.[159] The PSII functional model contains the *p*-benzoquinone derivative (X-Q) as a plastoquinone analog in $PhCH_3$ and a nonheme iron(II) complex ($[Fe^{II}(N_4Py)]^{2+}$; N_4Py = *N*,*N*-bis(2-pyridylmethyl)-*N*-bis(2-pyridyl)methylamine) as a H_2O oxidation catalyst in H_2O/TFE.[159] Photoirradiation of the PSII model cell resulted in production of the stoichiometric amount of O_2 and formation of a hydroquinone derivative (X-QH_2) that is a plastoquinol analog.[159] On the other hand, the PSI model cell contains nothing in $PhCH_3$, but X-QH_2, which is the product of the photocatalytic H_2O oxidation in the PSII model, Acr^+-Mes as a photoredox catalyst (a simple model of the photosynthetic reaction center for the charge separation),[47,160–162] and a cobalt(III) complex ($Co^{III}(dmgH)_2ClPy$) as an H_2 evolution catalyst in H_2O/TFE (3 : 1).[159] Photoirradiation of the PSI model cell resulted in evolution of the stoichiometric amount of H_2 and the formation of X-Q.[159] These PSI and PSII molecular models were

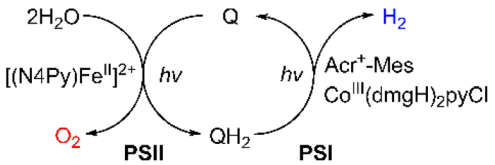

Scheme 18 Schematic diagram of light-driven H_2O splitting with the combination of PSI and PSII models. Reprinted from ref. 159 with permission from American Chemical Society (Copyright 2022).

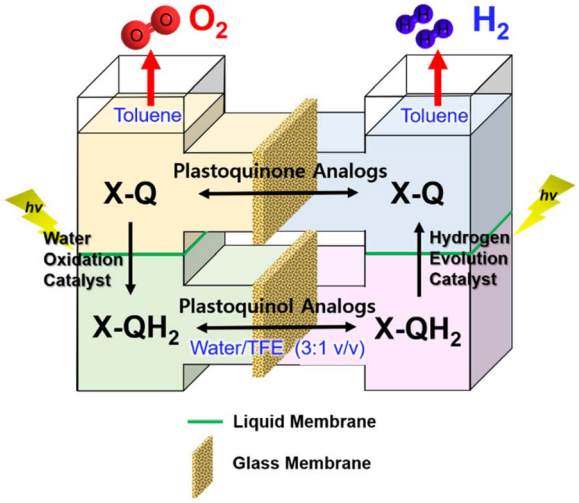

Fig. 8 An O-type photocatalytic cell for photocatalytic H_2O oxidation and reduction with a combination of PSI and PSII models. Reprinted from ref. 159 with permission from American Chemical Society (Copyright 2022).

combined through glass membranes to achieve overall water splitting to O_2 and H_2 in a 1 : 2 stoichiometric ratio under photoirradiation.[159] A TON of >100 has been achieved for the formation of H_2 by combining the PSI and PSII models, where X-Q acted as a photoredox catalyst in the photocatalytic H_2O splitting system as in the case of plastoquinone in photosynthesis.[159]

In the functional model of PSII, three steps of electron transfer from $[Fe^{II}(N_4Py)]^{2+}$ to X-Q*, which is the excited state of X-Q, generate an active intermediate ($[Fe^{V}(O)(N_4Py)]^{3+}$) which is able to oxidize H_2O to produce O_2 (Scheme 19).[163] In the functional model of PSI, electron transfer from X-QH_2 to ^{3}(Acr$^{\bullet}$-Mes$^{\bullet+}$)*, which is the triplet ET state of Acr$^+$-Mes, arises to form Acr$^{\bullet}$-Mes and $QH_2^{\bullet+}$ (Scheme 20).[164] $QH_2^{\bullet+}$ rapidly deprotonates to form QH$^{\bullet}$, accompanied by electron transfer from Acr$^{\bullet}$-Mes to $Co^{III}(dmgH)_2ClPy$ which produces $[Co^{II}(dmgH)_2ClPy]^-$ and regenerates Acr$^+$-Mes.[164] On the other hand, H-atom transfer from QH$^{\bullet}$ to $[Co^{II}(dmgH)_2ClPy]^-$ occurs to yield a cobalt(III)-hydride complex ($[Co^{III}(H)(dmgH)_2ClPy]^-$) that reacts with protons to produce H_2 and regenerate $Co^{III}(dmgH)_2ClPy$ (Scheme 20).[164] This is the first example of combining PSI and PSII functional models in solution to obtain photocatalytic H_2O splitting using a homogeneous molecular photocatalyst that produces O_2 and H_2 in a ratio of 1 : 2. Thus, this combinatorial system provides valuable mechanistic insights and reaction intermediates that are not possible using heterogeneous photocatalysts.[159]

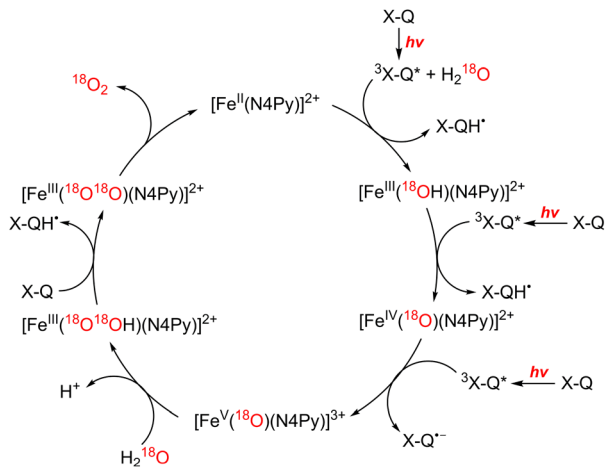

Scheme 19 Proposed mechanism of photocatalytic oxidation of water by X-Q with $[Fe^{II}(N_4Py)]^{2+}$. Reprinted from ref. 163 with permission from American Chemical Society (Copyright 2019).

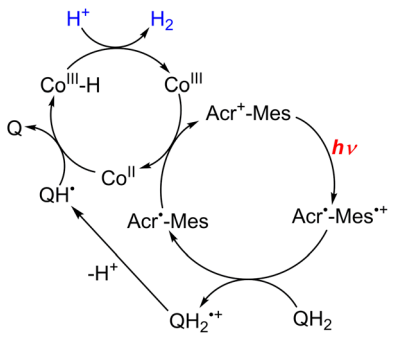

Scheme 20 Proposed mechanism of photocatalytic evolution of H_2 from X-QH_2 with Acr$^+$-Mes and $Co^{III}(dmgH)_2ClPy$. Reprinted from ref. 164 with permission from American Chemical Society (Copyright 2020).

Hydrogen produced in the PSI model can reduce NAD^+ to NADH as well as CO_2 to HCOOH with an Ir complex catalyst.[165] Therefore, the molecular photocatalytic H_2O splitting system (Fig. 8) can be applied to the generation of liquid solar fuels from H_2O and CO_2 by combining various catalysts reported for CO_2 reduction with H_2.[166–171] Combination of PSI and PSII models will enable the development of a variety of catalytic reduction reactions using water as an earth-abundant reductant.

7. Conclusion

Production of solar fuels from water requires multi-functional catalysts for photosensitization, water oxidation and reduction of O_2 to H_2O_2 or reduction of CO_2 to HCOOH, HCHO, CH_3OH *etc.* Coordination polymeric cyano (CN)-bridged heteronuclear metal complexes act as a dual functional photocatalyst for the photocatalytic production of H_2O_2 under visible light irradiation, catalyzing both photocatalytic oxidation of H_2O to O_2 and photocatalytic reduction of O_2 to H_2O_2. In particular, the combination of semiconductor photocatalysts and Prussian blue analogues provides a composite photocatalyst that exhibited improved photocatalytic performance for water oxidation. On the other hand, metal–organic frameworks (MOFs) and mesoporous cellular silica foams (MCFs) have provided effective scaffolds to accommodate photocatalysts and redox catalysts for visible-light-driven water oxidation, H_2 production, CO_2 reduction and H_2O_2 production by incorporating both organic parts and inorganic metal parts. New visible-light photocatalysts of MOFs and MCFs can be designed and synthesized by incorporating optically functionalized organic chromophores which is a feasible approach with high efficiency. Construction of a hybrid photoelectrochemical cell demonstrated solar fuel production from water and CO_2 with energy inputs from sunlight. Finally molecular models of PSII and PSII in photosynthesis were developed and they were combined with the use of liquid membranes to produce H_2 from H_2O under visible light photoirradiation through a quinone/hydroquinone redox couple as in the case of the plastoquinone/plastoquinone redox couple in photosynthesis. Such multi-functional molecular models of photosynthesis may hopefully pave a new and promising way for production of solar fuels more effectively than natural photosynthesis. In this review, bimetals play important roles in most multi-functional photocatalytic systems. Combination of coordination polymers, MOFs, COFs and MCFs with the use of multimetals may enable the construction of more efficient model systems of photosynthesis.

Conflicts of interest

There are no conflicts to declare.

Acknowledgements

The authors gratefully acknowledge the contributions of their collaborators and coworkers cited in the listed references and support from JSPS (No. 16H02268 and 23K04686 to S. F.) and NRF of Korea (NRF-2023R1A2C1007668 to Y.-M. L. and NRF-2021R1A3B1076539 to W. N.).

Notes and references

1 W. W. Fischer, J. Hemp and J. E. Johnson, *Annu. Rev. Earth Planet. Sci.*, 2016, **44**, 647–683.
2 N. S. Lewis, *Science*, 2016, **351**, aad1920.
3 T. Ahmad and D. Zhang, *Energy Rep.*, 2020, **6**, 1973–1991.
4 S. Fukuzumi, *Joule*, 2017, **1**, 689–738.
5 X. Tao, Y. Zhao, S. Wang, C. Li and R. Li, *Chem. Soc. Rev.*, 2022, **51**, 3561–3608.
6 Z. Wang, Y. Hu, S. Zhang and Y. Sun, *Chem. Soc. Rev.*, 2022, **51**, 6704–6737.
7 M. Thangamuthu, Q. Ruan, P. O. Ohemeng, B. Luo, D. Jing, R. Godin and J. Tang, *Chem. Rev.*, 2022, **122**, 11778–11829.
8 T. A. Faunce, W. Lubitz, A. W. Rutherford, D. MacFarlane, G. F. Moore, P. Yang, D. G. Nocera, T. A. Moore, D. H. Gregory, S. Fukuzumi, K. B. Yoon, F. A. Armstrong, M. R. Wasielewski and S. Styring, *Energy Environ. Sci.*, 2013, **6**, 695–698.
9 A. M. Appel, J. E. Bercaw, A. B. Bocarsly, H. Dobbek, D. L. DuBois, M. Dupuis, J. G. Ferry, E. Fujita, R. Hille, P. J. A. Kenis, C. A. Kerfeld, R. H. Morris, C. H. F. Peden, A. R. Portis, S. W. Ragsdale, T. B. Rauchfuss, J. N. H. Reek, L. C. Seefeldt, R. K. Thauer and G. L. Waldrop, *Chem. Rev.*, 2013, **113**, 6621–6658.
10 M. Aresta, A. Dibenedetto and A. Angelini, *Chem. Rev.*, 2014, **114**, 1709–1742.
11 K. A. Grice, *Coord. Chem. Rev.*, 2017, **336**, 78–95.
12 E. A. R. Cruz, D. Nishiori, B. L. Wadsworth, N. P. Nguyen, L. K. Hensleigh, D. Khusnutdinova, A. M. Beiler and G. F. Moore, *Chem. Rev.*, 2022, **122**, 16051–16109.
13 M. E. El-Khouly, E. El-Mohsnawy and S. Fukuzumi, *J. Photochem. Photobiol., C*, 2017, **31**, 36–83.
14 S. Fukuzumi, Y.-M. Lee and W. Nam, *Tetrahedron*, 2020, **76**, 131024.
15 A. Paul, S. D. Adhikary, S. Kapurwan and S. Konar, *J. Mater. Chem. A*, 2022, **10**, 13152–13169.
16 B. Zhang and L. Sun, *Chem. Soc. Rev.*, 2019, **48**, 2216–2264.
17 M. D. Kärkäs, O. Verho, E. V. Johnston and B. Åkermark, *Chem. Rev.*, 2014, **114**, 11863–12001.
18 J. S. O'Neill, L. Kearney, M. P. Brandon and M. T. Pryce, *Coord. Chem. Rev.*, 2022, **467**, 214599.
19 H. Sun, W. Ou, L. Sun, B. Wang and C. Su, *Nano Res.*, 2022, **15**, 10292–10315.
20 Q. Wang and K. Domen, *Chem. Rev.*, 2020, **120**, 919–985.
21 S. Chen, T. Takata and K. Domen, *Nat. Rev. Mater.*, 2017, **2**, 1–17.
22 U. V. Ghorpade, M. P. Suryawanshi, M. A. Green, T. Wu, X. Hao and K. M. Ryan, *Chem. Rev.*, 2023, **123**, 327–378.
23 Y. Fang, Y. Hou, X. Fu and X. Wang, *Chem. Rev.*, 2022, **122**, 4204–4256.
24 Z. Wang, C. Li and K. Domen, *Chem. Soc. Rev.*, 2019, **48**, 2109–2125.
25 X. Chen, S. Shen, L. Guo and S. S. Mao, *Chem. Rev.*, 2010, **110**, 6503–6570.
26 S. Yoshino, T. Takayama, Y. Yamaguchi, A. Iwase and A. Kudo, *Acc. Chem. Res.*, 2022, **55**, 966–977.
27 A. Kudo and Y. Miseki, *Chem. Soc. Rev.*, 2009, **38**, 253–278.
28 H. Yamashita, K. Mori, Y. Kuwahara, T. Kamegawa, M. Wen, P. Verma and M. Che, *Chem. Soc. Rev.*, 2018, **47**, 8072–8096.
29 J. Ran, J. Zhang, J. Yu, M. Jaroniec and S. Z. Qiao, *Chem. Soc. Rev.*, 2014, **43**, 7787–7812.
30 P. Niu, J. Dai, X. Zhi, Z. Xia, S. Wang and L. Li, *InfoMat*, 2021, **3**, 931–961.
31 Y. Guo, H. Li, W. Ma, W. Shi, Y. Zhu and W. Choi, *Carbon Energy*, 2020, **2**, 308–349.
32 A.-Y. Lo and F. Taghipour, *J. Mater. Chem. A*, 2021, **9**, 26430–26453.
33 A. Nakada, H. Kumagai, M. Robert, O. Ishitani and K. Maeda, *Acc. Mater. Res.*, 2021, **2**, 458–470.
34 F. Zaera, *Chem. Rev.*, 2022, **122**, 8594–8757.
35 S. Fukuzumi, Y.-M. Lee and W. Nam, *Coord. Chem. Rev.*, 2018, **355**, 54–73.
36 S. Fukuzumi, D. Hong and Y. Yamada, *J. Phys. Chem. Lett.*, 2013, **4**, 3458–3467.
37 S. Fukuzumi, Y.-M. Lee, H. S. Ahn and W. Nam, *Chem. Sci.*, 2018, **9**, 6017–6034.
38 R. Cauwenbergh and S. Das, *Green Chem.*, 2021, **23**, 2553–2574.
39 Y. Yamazaki, M. Miyaji and O. Ishitani, *J. Am. Chem. Soc.*, 2022, **144**, 6640–6660.
40 L. Wang and L. Wang, *Front. Chem.*, 2022, **10**, 996383.
41 Y. H. Hong, Y.-M. Lee, W. Nam and S. Fukuzumi, *ACS Catal.*, 2023, **13**, 308–341.
42 X. Li, H. Lei, L. Xie, N. Wang, W. Zhang and R. Cao, *Acc. Chem. Res.*, 2022, **55**, 878–892.
43 H. Lei, X. Li, J. Meng, H. Zheng, W. Zhang and R. Cao, *ACS Catal.*, 2019, **9**, 4320–4344.
44 D. L. Ashford, M. K. Gish, A. K. Vannucci, M. K. Brennaman, J. L. Templeton, J. M. Papanikolas and T. J. Meyer, *Chem. Rev.*, 2015, **115**, 13006–13049.
45 T. R. Cook, D. K. Dogutan, S. Y. Reece, Y. Surendranath, T. S. Teets and D. G. Nocera, *Chem. Rev.*, 2010, **110**, 6474–6502.
46 N. Armaroli and V. Balzani, *Chem.–Eur. J.*, 2016, **22**, 32–57.
47 S. Fukuzumi, K. Ohkubo and T. Suenobu, *Acc. Chem. Res.*, 2014, **47**, 1455–1464.
48 S. Fukuzumi, *Curr. Opin. Chem. Biol.*, 2015, **25**, 18–26.
49 K. Sakai and H. Ozawa, *Coord. Chem. Rev.*, 2007, **251**, 2753–2766.
50 H. Ozawa and K. Sakai, *Chem. Commun.*, 2011, **47**, 2227–2242.
51 K. L. Skubi, T. R. Blum and T. P. Yoon, *Chem. Rev.*, 2016, **116**, 10035–10074.

52 K. R. Bajya and S. Selvakumar, *Eur. J. Org. Chem.*, 2022, **2022**, e202200229.
53 L. Qin, R. Wang, X. Xin, M. Zhang, T. Liu, H. Lv and G.-Y. Yang, *Appl. Catal., B*, 2022, **312**, 121386.
54 Q. Zhang and C. Wang, *Eur. J. Org. Chem.*, 2022, **2022**, e202200431.
55 T. E. Schirmer and B. König, *J. Am. Chem. Soc.*, 2022, **144**, 19207–19218.
56 E. B. McLean and A.-L. Lee, *Tetrahedron*, 2018, **74**, 4881–4902.
57 R. Ham, C. J. Nielsen, S. Pullen and J. N. H. Reek, *Chem. Rev.*, 2023, **123**, 5225–5261.
58 S. Kato, J. Jung, T. Suenobu and S. Fukuzumi, *Energy Environ. Sci.*, 2013, **6**, 3756–3764.
59 S. Fukuzumi, Y.-M. Lee and W. Nam, *Chem.–Eur. J.*, 2018, **24**, 5016–5031.
60 C. J. McDonnell-Worth and D. R. MacFarlane, *Aust. J. Chem.*, 2018, **71**, 781–788.
61 S. Fukuzumi, *Biochim. Biophys. Acta*, 2016, **1857**, 604–611.
62 Y. Yamada, M. Yoneda and S. Fukuzumi, *Energy Environ. Sci.*, 2015, **8**, 1698–1701.
63 S. Fukuzumi and Y. Yamada, *ChemElectroChem*, 2016, **3**, 1978–1989.
64 L. An, T. Zhao, X. Yan, X. Zhou and P. Tan, *Sci. Bull.*, 2015, **60**, 55–64.
65 S. Fukuzumi and Y. Yamada, *Aust. J. Chem.*, 2014, **67**, 354–364.
66 S. Fukuzumi, Y. Yamada and K. D. Karlin, *Electrochim. Acta*, 2012, **82**, 493–511.
67 H. Hou, X. Zeng and X. Zhang, *Angew. Chem., Int. Ed.*, 2020, **59**, 17356–17376.
68 Y. Sun, L. Han and P. Strasser, *Chem. Soc. Rev.*, 2020, **49**, 6605–6631.
69 X. Hu, X. Zeng, Y. Liu, J. Lu and X. Zhang, *Nanoscale*, 2020, **12**, 16008–16027.
70 Y.-X. Ye, C. Wen, J. Pan, J.-W. Wang, Y.-J. Tong, S. Wei, Z. Ke, L. Jiang, F. Zhu, N. Zhou, M. Zhou, J. Xu and G. Ouyang, *Appl. Catal., B*, 2021, **285**, 119726.
71 Y. Aratani, T. Suenobu, K. Ohkubo, Y. Yamada and S. Fukuzumi, *Chem. Commun.*, 2017, **53**, 3473–3476.
72 T. Zhang and W. Lin, *Chem. Soc. Rev.*, 2014, **43**, 5982–5993.
73 C. Wang, K. E. deKrafft and W. Lin, *J. Am. Chem. Soc.*, 2012, **134**, 7211–7214.
74 Y. Horiuchi, T. Toyao, M. Saito, K. Mochizuki, M. Iwata, H. Higashimura, M. Anpo and M. Matsuoka, *J. Phys. Chem. C*, 2012, **116**, 20848–20853.
75 T. Toyao, M. Saito, S. Dohshi, K. Mochizuki, M. Iwata, H. Higashimura, Y. Horiuchi and M. Matsuoka, *Chem. Commun.*, 2014, **50**, 6779–6781.
76 Y. Aratani, K. Oyama, T. Suenobu, Y. Yamada and S. Fukuzumi, *Inorg. Chem.*, 2016, **55**, 5780–5786.
77 Y. Isaka, S. Kato, D. Hong, T. Suenobu, Y. Yamada and S. Fukuzumi, *J. Mater. Chem. A*, 2015, **3**, 12404–12412.
78 Y. Isaka, K. Oyama, Y. Yamada, T. Suenobu and S. Fukuzumi, *Catal. Sci. Technol.*, 2016, **6**, 681–684.
79 S. S. Akbari, U. Unal and F. Karadas, *ACS Appl. Energy Mater.*, 2021, **4**, 12383–12390.
80 J. Zhou, W. Chen, C. Sun, L. Han, C. Qin, M. Chen, X. Wang, E. Wang and Z. Su, *ACS Appl. Mater. Interfaces*, 2017, **9**, 11689–11695.
81 D. Zhou and B.-H. Han, *Adv. Funct. Mater.*, 2010, **20**, 2717–2722.
82 J. Li, W. Chen, L. Chen, X. Zheng, G. Zhu and E. Wang, *Adv. Opt. Mater.*, 2018, **6**, 1800225.
83 Y. Liu, C. Tang, M. Cheng, M. Chen, S. Chen, L. Lei, Y. Chen, H. Yi, Y. Fu and L. Li, *ACS Catal.*, 2021, **11**, 13374–13396.
84 G. Paille, M. Gomez-Mingot, C. Roch-Marchal, B. Lassalle-Kaiser, P. Mialane, M. Fontecave, C. Mellot-Draznieks and A. Dolbecq, *J. Am. Chem. Soc.*, 2018, **140**, 3613–3618.
85 G. Paille, M. Gomez-Mingot, C. Roch-Marchal, M. Haouas, Y. Benseghir, T. Pino, M.-H. Ha-Thi, G. Landrot, P. Mialane, M. Fontecave, A. Dolbecq and C. Mellot-Draznieks, *ACS Appl. Mater. Interfaces*, 2019, **11**, 47837–47845.
86 S. Pullen, H. Fei, A. Orthaber, S. M. Cohen and S. Ott, *J. Am. Chem. Soc.*, 2013, **135**, 16997–17003.
87 D.-Y. Du, J.-S. Qin, S.-L. Li, Z.-M. Su and Y.-Q. Lan, *Chem. Soc. Rev.*, 2014, **43**, 4615–4632.
88 X.-X. Li, J. Liu, L. Zhang, L.-Z. Dong, Z.-F. Xin, S.-L. Li, X.-Q. Huang-Fu, K. Huang and Y.-Q. Lan, *ACS Appl. Mater. Interfaces*, 2019, **11**, 25790–25795.
89 Y. Benseghir, A. Lemarchand, M. Duguet, P. Mialane, M. Gomez-Mingot, C. Roch-Marchal, T. Pino, M.-H. Ha-Thi, M. Haouas, M. Fontecave, A. Dolbecq, C. Sassoye and C. Mellot-Draznieks, *J. Am. Chem. Soc.*, 2020, **142**, 9428–9438.
90 K. Zhang, S. Goswami, H. Noh, Z. Lu, T. Sheridan, J. Duan, W. Dong and J. T. Hupp, *J. Photochem. Photobiol.*, 2022, **10**, 100111.
91 J. Bonin, M. Chaussemier, M. Robert and M. Routier, *ChemCatChem*, 2014, **6**, 3200–3207.
92 B. Probst, A. Rodenberg, M. Guttentag, P. Hamm and R. Alberto, *Inorg. Chem.*, 2010, **49**, 6453–6460.
93 H. Zhang, J. Wei, J. Dong, G. Liu, L. Shi, P. An, G. Zhao, J. Kong, X. Wang, X. Meng, J. Zhang and J. Ye, *Angew. Chem., Int. Ed. Engl.*, 2016, **55**, 14310–14314.
94 P. Du, J. Schneider, P. Jarosz and R. Eisenberg, *J. Am. Chem. Soc.*, 2006, **128**, 7726–7727.
95 D. Chen, H. Xing, C. Wang and Z. Su, *J. Mater. Chem. A*, 2016, **4**, 2657–2662.
96 Y. Isaka, Y. Kondo, Y. Kawase, Y. Kuwahara, K. Mori and H. Yamashita, *Chem. Commun.*, 2018, **54**, 9270–9273.
97 Y. Fu, D. Sun, Y. Chen, R. Huang, Z. Ding, X. Fu and Z. Li, *Angew. Chem., Int. Ed.*, 2012, **51**, 3364–3367.
98 L. Shen, M. Luo, L. Huang, P. Feng and L. Wu, *Inorg. Chem.*, 2015, **54**, 1191–1193.
99 J.-N. Chang, Q. Li, J.-W. Shi, M. Zhang, L. Zhang, S. Li, Y. Chen, S.-L. Li and Y.-Q. Lan, *Angew. Chem., Int. Ed.*, 2023, **62**, e202218868.
100 S. Porcu, F. Secci and P. C. Ricci, *Molecules*, 2022, **27**, 6828.
101 Y. Wu, T. Sakurai, T. Adachi and Q. Wang, *Nanoscale*, 2023, **15**, 6521–6535.

102 H. Song, L. Wei, L. Chen, H. Zhang and J. Su, *Top. Catal.*, 2020, **63**, 895–912.
103 C. Gérardin, J. Reboul, M. Bonne and B. Lebeau, *Chem. Soc. Rev.*, 2013, **42**, 4217–4255.
104 I. Sierra and D. Pérez-Quintanilla, *Chem. Soc. Rev.*, 2013, **42**, 3792–3807.
105 P. Yang, S. Gai and J. Lin, *Chem. Soc. Rev.*, 2012, **41**, 3679–3698.
106 S.-H. Wu, C.-Y. Mou and H.-P. Lin, *Chem. Soc. Rev.*, 2013, **42**, 3862–3875.
107 H. Wang, Q. Tang, Z. Chen, T. Li and J. Wang, *Sci. China Mater.*, 2020, **63**, 2189–2205.
108 H. Jung, Y. Whang and S. W. Han, *Bull. Korean Chem. Soc.*, 2021, **42**, 806–809.
109 X. Qian, K. Fuku, Y. Kuwahara, T. Kamegawa, K. Mori and H. Yamashita, *ChemSusChem*, 2014, **7**, 1528–1536.
110 C. Cheng, D. Lu, B. Shen, Y. Liu, J. Lei, L. Wang, J. Zhang and M. Matsuoka, *Microporous Mesoporous Mater.*, 2016, **226**, 79–87.
111 H. Y. Kim, J. Y. Kim and S. H. Joo, *Bull. Korean Chem. Soc.*, 2021, **42**, 724–736.
112 J. G. Mahy, C. A. Paez, C. Carcel, C. Bied, A. S. Tatton, C. Damblon, B. Heinrichs, M. Wong Chi Man and S. D. Lambert, *J. Photochem. Photobiol., A*, 2019, **373**, 66–76.
113 P. Rana, B. Kaushik, K. Solanki, K. Mohan Saini and R. K. Sharma, *Chem. Commun.*, 2022, **58**, 11354–11377.
114 A. A. Yakushev, A. S. Abel, A. D. Averin, I. P. Beletskaya, A. V. Cheprakov, I. S. Ziankou, L. Bonneviot and A. Bessmertnykh-Lemeune, *Coord. Chem. Rev.*, 2022, **458**, 214331.
115 S. Lin, H. Huang, T. Ma and Y. Zhang, *Adv. Sci.*, 2021, **8**, 2002458.
116 M. Waki, S. Shirai, K.-I. Yamanaka, Y. Maegawa and S. Inagaki, *RSC Adv.*, 2020, **10**, 13960–13967.
117 Y. Yamada, H. Tadokoro, M. Naqshbandi, J. Canning, M. J. Crossley, T. Suenobu and S. Fukuzumi, *ChemPlusChem*, 2016, **81**, 521–525.
118 S. Zhang, M. Li, Q. Wu, H. Yang, J. Han, H. Wang and X. Liu, *Appl. Catal., B*, 2018, **236**, 466–474.
119 T. Jin, C. Liu and G. Li, *J. Coord. Chem.*, 2016, **69**, 1748–1758.
120 Y. Ueda, H. Takeda, T. Yui, K. Koike, Y. Goto, S. Inagaki and O. Ishitani, *ChemSusChem*, 2015, **8**, 439–442.
121 H. Kumagai, Y. Tamaki and O. Ishitani, *Acc. Chem. Res.*, 2022, **55**, 978–990.
122 S. Fukuzumi, K. Doi, A. Itoh, T. Suenobu, K. Ohkubo, Y. Yamada and K. D. Karlin, *Proc. Natl. Acad. Sci. U. S. A.*, 2012, **109**, 15572–15577.
123 K. Ohkubo, K. Mizushima, R. Iwata, K. Souma, N. Suzuki and S. Fukuzumi, *Chem. Commun.*, 2010, **46**, 601–603.
124 T. Arai, S. Sato and T. Morikawa, *Energy Environ. Sci.*, 2015, **8**, 1998–2002.
125 T. Arai, S. Sato, K. Uemura, T. Morikawa, T. Kajino and T. Motohiro, *Chem. Commun.*, 2010, **46**, 6944–6946.
126 S. Sato, T. Arai, T. Morikawa, K. Uemura, T. M. Suzuki, H. Tanaka and T. Kajino, *J. Am. Chem. Soc.*, 2011, **133**, 15240–15243.
127 K. Maeda, R. Kuriki, M. Zhang, X. Wang and O. Ishitani, *J. Mater. Chem. A*, 2014, **2**, 15146–15151.
128 R. Kuriki, O. Ishitani and K. Maeda, *ACS Appl. Mater. Interfaces*, 2016, **8**, 6011–6018.
129 A. Nakada, T. Nakashima, K. Sekizawa, K. Maeda and O. Ishitani, *Chem. Sci.*, 2016, **7**, 4364–4371.
130 K. Wada, M. Eguchi, O. Ishitani and K. Maeda, *ChemSusChem*, 2017, **10**, 287–295.
131 R. Kuriki, H. Matsunaga, T. Nakashima, K. Wada, A. Yamakata, O. Ishitani and K. Maeda, *J. Am. Chem. Soc.*, 2016, **138**, 5159–5170.
132 H. Kumagai, G. Sahara, K. Maeda, M. Higashi, R. Abe and O. Ishitani, *Chem. Sci.*, 2017, **8**, 4242–4249.
133 M. Shizuno, K. Kato, S. Nishioka, T. Kanazawa, D. Saito, S. Nozawa, A. Yamakata, O. Ishitani and K. Maeda, *ACS Appl. Energy Mater.*, 2022, **5**, 9479–9486.
134 M. A. Gross, C. E. Creissen, K. L. Orchard and E. Reisner, *Chem. Sci.*, 2016, **7**, 5537–5546.
135 J. Massin, M. Bräutigam, N. Kaeffer, N. Queyriaux, M. J. Field, F. H. Schacher, J. Popp, M. Chavarot-Kerlidou, B. Dietzek and V. Artero, *Interface Focus*, 2015, **5**, 20140083.
136 B. Samanta, Á. Morales-García, F. Illas, N. Goga, J. A. Anta, S. Calero, A. Bieberle-Hütter, F. Libisch, A. B. Muños-García, M. Pavone and M. C. Toroker, *Chem. Soc. Rev.*, 2022, **51**, 3794–3818.
137 M. Grätzel, *Acc. Chem. Res.*, 1981, **14**, 376–384.
138 A. J. Bard and M. A. Fox, *Acc. Chem. Res.*, 1995, **28**, 141–145.
139 D. Gust, T. A. Moore and A. L. Moore, *Acc. Chem. Res.*, 2009, **42**, 1890–1898.
140 Y. Tachibana, L. Vayssieres and J. R. Durrant, *Nat. Photonics*, 2012, **6**, 511–518.
141 F. E. Osterloh, *Chem. Soc. Rev.*, 2013, **42**, 2294–2320.
142 Y. Qu and X. Duan, *Chem. Soc. Rev.*, 2013, **42**, 2568–2580.
143 T. Hisatomi, J. Kubota and K. Domen, *Chem. Soc. Rev.*, 2014, **43**, 7520–7535.
144 C. Jiang, S. J. A. Moniz, A. Wang, T. Zhang and J. Tang, *Chem. Soc. Rev.*, 2017, **46**, 4645–4660.
145 S. Chen, T. Takata and K. Domen, *Nat. Rev. Mater.*, 2017, **2**, 17050.
146 J. Yano and V. Yachandra, *Chem. Rev.*, 2014, **114**, 4175–4205.
147 J. Barber, *Chem. Soc. Rev.*, 2009, **38**, 185–196.
148 J. P. McEvoy and G. W. Brudvig, *Chem. Rev.*, 2006, **106**, 4455–4483.
149 H. Dau and I. Zaharieva, *Acc. Chem. Res.*, 2009, **42**, 1861–1870.
150 N. Cox, D. A. Pantazis, F. Neese and W. Lubitz, *Acc. Chem. Res.*, 2013, **46**, 1588–1596.
151 F. Rappaport, M. Guergova-Kuras, P. J. Nixon, B. A. Diner and J. Lavergne, *Biochemistry*, 2002, **41**, 8518–8527.
152 J. M. Keough, A. N. Zuniga, D. L. Jenson and B. A. Barry, *J. Phys. Chem. B*, 2013, **117**, 1296–1307.
153 L. A. Malone, M. S. Proctor, A. Hitchcock, C. N. Hunter and M. P. Johnson, *Biochim. Biophys. Acta, Bioenerg.*, 2021, **1862**, 148380.
154 S. Wada, Y. Suzuki and C. Miyake, *Plants*, 2020, **9**, 319.
155 C. Miyake, *Antioxidants*, 2020, **9**, 230.

156 T. G. Laughlin, A. N. Bayne, J.-F. Trempe, D. F. Savage and K. M. Davies, *Nature*, 2019, **566**, 411–414.
157 J. Z. Zhang and E. Reisner, *Nat. Rev. Chem.*, 2020, **4**, 6–21.
158 H. Kubota-Kawai, R. Mutoh, K. Shinmura, P. Sétif, M. M. Nowaczyk, M. Rögner, T. Ikegami, H. Tanaka and G. Kurisu, *Nat. Plants*, 2018, **4**, 218–224.
159 Y. H. Hong, Y.-M. Lee, W. Nam and S. Fukuzumi, *J. Am. Chem. Soc.*, 2022, **144**, 695–700.
160 S. Fukuzumi, H. Kotani, K. Ohkubo, S. Ogo, N. V. Tkachenko and H. Lemmetyinen, *J. Am. Chem. Soc.*, 2004, **126**, 1600–1601.
161 T. Tsudaka, H. Kotani, K. Ohkubo, T. Nakagawa, N. V. Tkachenko, H. Lemmetyinen and S. Fukuzumi, *Chem.–Eur. J.*, 2017, **23**, 1306–1317.
162 S. Fukuzumi, Y.-M. Lee and W. Nam, *Biochem. Soc. Trans.*, 2018, **46**, 1279–1288.
163 Y. H. Hong, J. Jung, T. Nakagawa, N. Sharma, Y.-M. Lee, W. Nam and S. Fukuzumi, *J. Am. Chem. Soc.*, 2019, **141**, 6748–6754.
164 Y. H. Hong, Y.-M. Lee, W. Nam and S. Fukuzumi, *Inorg. Chem.*, 2020, **59**, 14838–14846.
165 Y. Maenaka, T. Suenobu and S. Fukuzumi, *J. Am. Chem. Soc.*, 2012, **134**, 367–374.
166 C. Liu, B. C. Colón, M. Ziesack, P. A. Silver and D. G. Nocera, *Science*, 2016, **352**, 1210–1213.
167 W. Tu, Y. Zhou and Z. Zou, *Adv. Mater.*, 2014, **26**, 4607–4626.
168 E. Nikoloudakis, I. López-Duarte, G. Charalambidis, K. Ladomenou, M. Ince and A. G. Coutsolelos, *Chem. Soc. Rev.*, 2022, **51**, 6965–7045.
169 H. Hayashi, S. Ogo and S. Fukuzumi, *Chem. Commun.*, 2004, 2714–2715.
170 Y. Maenaka, T. Suenobu and S. Fukuzumi, *Energy Environ. Sci.*, 2012, **5**, 7360–7367.
171 K. Kamada, J. Jung, T. Wakabayashi, K. Sekizawa, S. Sato, T. Morikawa, S. Fukuzumi and S. Saito, *J. Am. Chem. Soc.*, 2020, **142**, 10261–10266.